FULL RESEARCH ARTICLE

Manufacturing oxide-dispersion-strengthened steels using the advanced directed energy deposition process of high-speed laser cladding

Markus B. Wilms[1,2] [iD] **· Norbert Pirch[2] · Bilal Gökce[3]**

Abstract

In this work, we demonstrate the feasibility of manufacturing an iron-based oxide-dispersion-strengthened (ODS) PM2000 composite material with the chemical composition of $Fe20Cr4.5Al0.5Ti + 0.5Y_2O_3$ (in wt.%) via the advanced directed energy deposition (DED) process of high-speed laser cladding (HSLC). The characteristic high solidification rates of HSLC processes allow the successful dispersion of nano-scaled yttrium-based oxides in the ferritic stainless steel matrix. The effective suppression of nano-particle agglomeration during the melting stage, which is frequently observed in conventional DED processes of ODS materials, is reflected by smaller dispersoid sizes and corresponding higher hardness of manufactured specimen compared to DED-manufactured counterparts.

1 Introduction

Oxide-dispersion-strengthened (ODS) materials are promising candidate materials for new GenIV nuclear reactors due to their tolerance toward irradiation-induced defects [1–3]. In addition, this material class offers superior mechanical properties at room and elevated temperatures [4–7]. Therefore, ODS materials are also considered for applications in the fields of stationary gas turbines or combustion engines in the aerospace industry [8].

ODS materials gain their outstanding mechanical properties typically from the presence of sub-micrometer-sized oxide particles that are homogeneously distributed in a corrosion-resistant metallic matrix. Manufacturing of ODS steels is typically performed via a mechanical alloying process by ball milling [9, 10], followed by compaction via hot extrusion or hot isostatic pressing (HIP), subsequent hot rolling, and subtractive manufacturing [11, 12]. Apart from this powder metallurgical route, only few alternative concepts enabling the successful dispersion of nanometer-sized oxides in a metallic matrix have been reported, such as the gas atomization reaction synthesis followed by internal oxidation reaction during HIP [13] or in-situ oxidation of a titanium wire introduced into a steel melt under severe electromagnetic stirring [14]. Other promising approaches are based on gas synthesis formation of oxides in a melt pool, internal oxidation [15, 16], spark plasma sintering (SPS) [17, 18]. However, most of these processes only allow the production of simply shaped bodies and need costly subtractive manufacturing before being applied in a particular application.

Laser additive manufacturing (LAM) is principally capable of producing highly complex parts directly from computer files and raw material powders. LAM processes are characterized by small melt pool dimensions with high solidification rates in combination with complex flow patterns due to the so-called marangoni forces or with the formation

✉ Markus B. Wilms
  mwilms@uni-wuppertal.de

[1] Materials Science and Additive Manufacturing, School of Mechanical Engineering and Safety Engineering, University of Wuppertal, Gaußstr. 20, 42119 Wuppertal, Germany

[2] Fraunhofer Institute for Laser Technology ILT, Steinbachstr. 15, 52074 Aachen, Germany

[3] Materials Science and Additive Manufacturing, School of Mechanical Engineering and Safety Engineering, University of Wuppertal, Gaußstr. 20, 42119 Wuppertal, Germany

of a keyhole due to the displacement flow, resulting in effective dispersion of nano-scaled oxide particles. In the literature, the feasibility of the LAM-method of laser powder bed fusion (L-PBF), also termed as selective laser melting (SLM), for the manufacturing of various ODS alloys has been demonstrated using mechanically alloyed powder material as a feedstock [19–24]. An approach utilizing laser-processed powder material containing the metallic and ceramic components of the alloy as a feedstock also has been demonstrated. [25–28] For the LAM process of directed energy deposition (DED), also referred to as laser metal deposition (LMD), general feasibility has been demonstrated using mechanically alloyed powder material [29–31]. However, pronounced agglomeration and clustering of oxide nanoparticles in DED-manufactured material are observed [32, 33], resulting in the dispersion of agglomerated oxide dispersoids with reduced number densities compared to L-PBF processed material. [27] The agglomeration tendencies are attributed to reduced solidification and cooling rates, which stem from larger beam diameters and lower process velocities used in DED processes compared to L-PBF processes [27] or the utility of additional preheating [29, 34].

In the present work, we demonstrate the feasibility of the advanced DED process of high-speed laser cladding (HSLC), a next-generation coating and repair technology for large-scaled metallic components [35–37] to synthesize a highly corrosion-resistant Fe-based ODS alloy, designated as PM2000 (Fe20Cr4.5Al0.5Ti + 0.5 Y_2O_3 (wt.%)) and characterized by a ferritic stainless steel matrix and homogeneously dispersed nano-scaled yttrium-based oxides. [38] HSLC offers higher solidification rates of up to 10^6 K/s [39] compared to conventional DED processes with approx. 10^4 K/s [27, 40] and therefore is considered to significantly reduce agglomeration tendencies of nano-scaled oxides during the melting stage, frequently observed in DED processed PM2000 material [25–29].

2 Experimental procedure

2.1 Powder material

The used metallic powder materials Fe20Cr4.5Al0.5Ti (wt.%) were received in an Ar-atomized state (Nanoval GmbH, Berlin, Germany) in a particle size distribution of 15–45 μm with a d_{50} value of 32.1 μm (Fig. 1a) according to the manufacturer. Y_2O_3 powder (abcr GmbH, Karlsruhe, Germany) was received in a particle fraction of 20–40 nm. Due to massive agglomeration by electrostatic forces, nanometer-sized powder material cannot be conveyed via conventional powder feeding systems, which makes the manufacturing of a powder compound consisting of micrometer-sized metallic powder and nanometer-sized powder necessary. Manufacturing of a powder compound was performed via mechanical alloying in the planetary mill Pulverisette 4 classic line (Fritsch GmbH, Idar-Oberstein, Germany) using milling containers and grinding balls manufactured from yttrium stabilized zirconia (YSZ). The result was a powder compound consisting of metallic particles covered with nanometer-scaled Y_2O_3 particles on the surface. Only minor deformation of the metallic particles by the milling process was observed; hence, the powder compound was considered suitable for the used powder feed system (Fig. 1b).

EDS measurements on the surface of the powder particles shown in Table 1 confirm the presence of yttrium and oxygen on the surface of the mechanically alloyed powder material.

2.2 High-speed laser cladding (HSLC)

The HSLC process was performed using a 4-axis gantry system equipped with a fiber-coupled diode laser system LDF 2000-30 (Laserline GmbH, Mülheim-Kärlich,
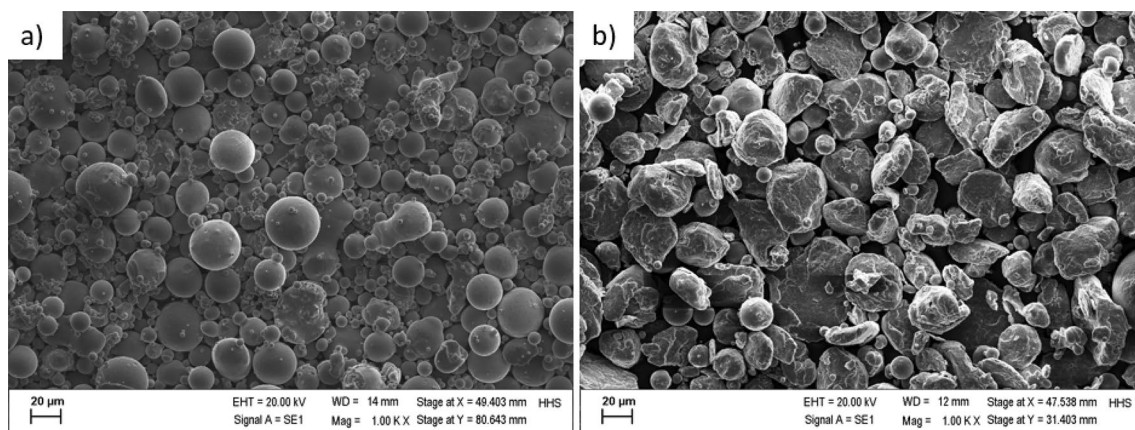
Fig. 1 SEM images of powder particles: **a** Gas-atomized Fe20Cr4.5Al0.5Ti (wt.%), **b** Mechanically alloyed Fe20Cr4.5Al0.5Ti + 0.5% Y_2O_3 (wt.%)

Table 1 EDS measurements (wt.%) on the surface of the powder particles

Element	Fe	Cr	Al	Ti	Y	O
Gas-atomized powder	74.72	21.11	5.13	0.59	–	–
Mechanically alloyed powder	73.54	19.92	4.13	0.57	1.79	2.53
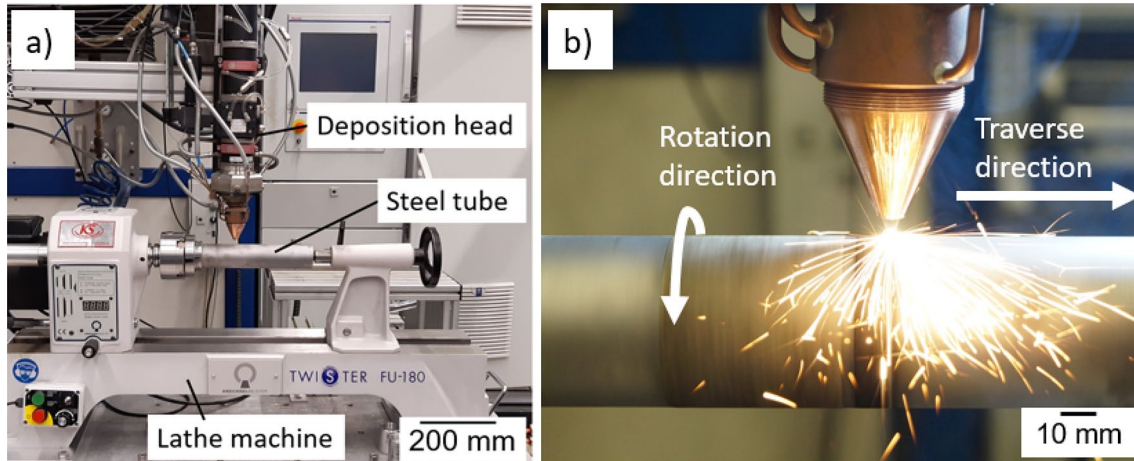
Fig. 2 Overview of the machine setup and HSLC process. **a** Photograph showing the general machine setup with deposition head equipped with a continuous coaxial powder nozzle and lathe machine with steel tube positioned 8.5 mm below the nozzle tip. **b** Photograph of the HSLC process during deposition of the mechanically alloyed powder material Fe20Cr4.5Al0.5Ti + 0.5% Y_2O_3 (wt.%)

Germany) emitting laser radiation with wavelengths of 1025 nm and 1064 nm simultaneously. The laser beam was guided by an optical fiber and shaped via collimation ($f_c = 200$ mm) and focusing lens ($f_f = 182$ mm) to generate a focal spot with a diameter of approx. 0.6 mm and a top-hat beam profile. The powder material was fed by conventional disk-based powder feeding units PF 2/2 (GTV Verschleißschutz GmbH, Luckenbach, Germany) via Argon carrier gas. Before entering the powder nozzle, the powder gas stream entered a diffusor unit dividing the powder gas stream into three independent streams to homogenously feed the powder material into the continuous coaxial powder nozzle D40 (Fraunhofer ILT, Aachen), injecting the powder material into the melt pool formed by the laser beam on the substrate surface. A local argon shielding gas atmosphere was created by the coaxial powder nozzle to protect the melt pool from atmospheric oxidation (Fig. 2).

As a substrate material, steel tubes (AISI 304) with a wall thickness of 5 mm and an outer diameter of 50 mm were used, which were mounted on a lathe machine Twister FU-180 (Neureiter Maschinen GmbH, Kuchl bei Salzburg, Austria). The substrates were sand-blasted and cleaned with ethanol before mounting to avoid surface contaminations. The process parameters for the HSLC process used are shown in Table 2.

Table 2 Process parameters for HSLC process of Fe20Cr4.5Al0.5Ti (wt.%) base alloy and its ODS counterparts

Laser power [W]	Rotation speed [rpm]	Traverse speed [mm/min]	Powder feed [g/min]	Beam diameter [mm]	Shielding/Carrier gas flow [l/min]
1099	150	45	5.33	0.66	15 / 7

2.3 Melt pool simulations

The determination of the temperature distribution and the solidification kinetics during the HSLC process was performed via simulations. The simulation is based on a mathematical model operating with the integration of the time-dependent heat equations in conjuction with calculations of the track geometry using nonlinear Young–Laplace equations and solved with the finite element method (FEM) [27]. Temperature-dependent thermophysical data for heat capacity, thermal conductivity, and thermal expansion were taken from Kanthal APMT FeCrAl-based steel [41]. A density of 7.25 g/cm^3 [42] is

used for modeling. Due to their small volume fraction, the influence of the dispersed nanoparticles was considered negligible for the FEM melt pool simulations.

3 Characterization methods

The microstructural characterization was performed by standard metallographic analysis. Specimens were cut parallel to the traverse direction and embedded in a conductive resin followed by grinding with SiC paper and final polishing procedure using 1 µm diamond suspension. For visualization of the microstructure during the examinations using light optical microscopy (LOM) and scanning electron microscopy (SEM), the cross sections were etched for approx. 30 s using Nital etchant (3 vol.% HNO_3 in ethanol).

SEM imaging of the powder particles was performed on a Zeiss Leo 1455EP equipped with an Oxford Instruments EDS detector. A minimum of two individual point measurements on 15 randomly selected powder particles were taken to determine the chemical composition. SEM imagery in SE mode and EDS was performed at an acceleration voltage of 20 kV. SEM images of samples manufactured by high-speed laser cladding were acquired using an FEI FEG XL30 in SE mode with an acceleration voltage of 15 kV.

Hardness measurements along the build direction were performed using a Qness Q30 A + (ATM Qness GmbH, Mammelzen, Germany) in Vickers mode with a load of 0.1 kg. Mean hardness values are calculated from six individual indents at every build height measured.

4 Results and discussion

4.1 Microstructural characterization

Figure 3 provides LOM images of cross sections consisting of two subsequently manufactured layers for both material types. The non-reinforced coating, manufactured with Fe20Cr4.5Al0.5Ti (wt.%) material, (Fig. 3a) features full metallurgical bonding to the substrate material without any sign of delamination or defects in the fusion zone. The full double-layered coatings are found to be almost defect-free, exhibiting no cracks and low porosity, resulting in a relative density of 99.94%. The curvature of the fusion zone proves that substantial melting of substrate material occurred, resulting in an effective layer height of approx. 100 µm. The fact that the upper layer exhibits a larger layer height indicates significant remelting of the previously applied layer.

A strong texture in building direction (BD) is observed, indicating that the main heat diffusion direction is perpendicular to the building direction. The inclination of the grain growth direction of grains starting at the substrate–cladding interface is caused by the curvature of the melt pool [43, 44]. The curvature of the melt pool is directly connected with the melt pool geometry and describes the solid–liquid interface from the bottom to the surface of the melt pool during the deposition process. [45]

The grain growth direction is not altered by the layer boundary (indicated by the red line), and epitaxial grain growth (indicated by purple arrows) is observed regularly. However, the growth direction changes significantly parallel to the traverse direction in the top area of the cladding (indicated by blue arrows). The abrupt change of the grain growth orientation can be explained by the curvature of the
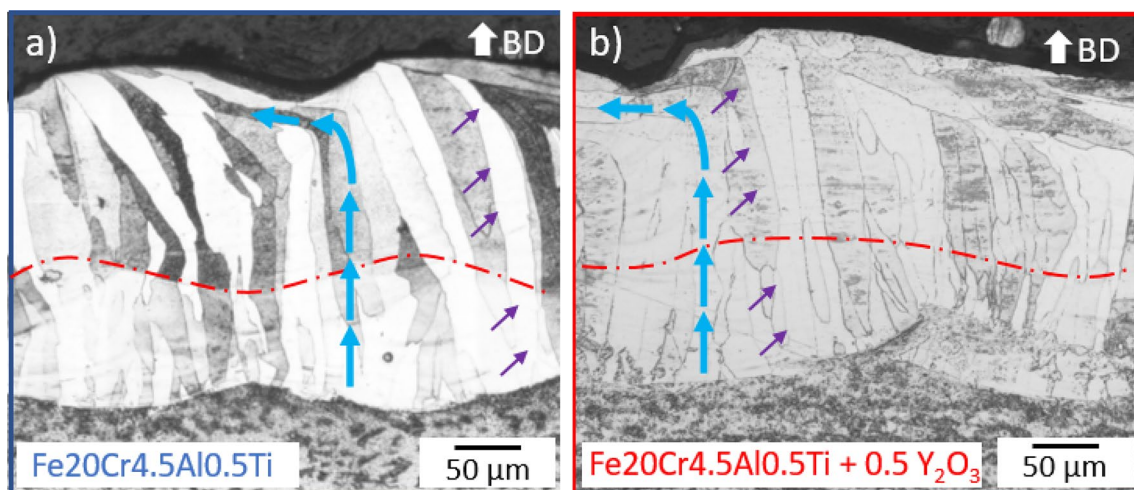
Fig. 3 LOM images of etched cross sections of non-reinforced (**a**) and reinforced coatings (**b**)

melt pool boundary and the energetically preferred growth direction, which is the smallest angle to the temperature gradient [44]. Because all these features can also be observed in the cladding manufactured with Fe20Cr4.5Al0.5Ti+0.5% Y_2O_3 (wt.%) (Fig. 3b), it can be concluded that no apparent change between reinforced and non-reinforced cladding could be observed on a scale that can be resolved by LOM.
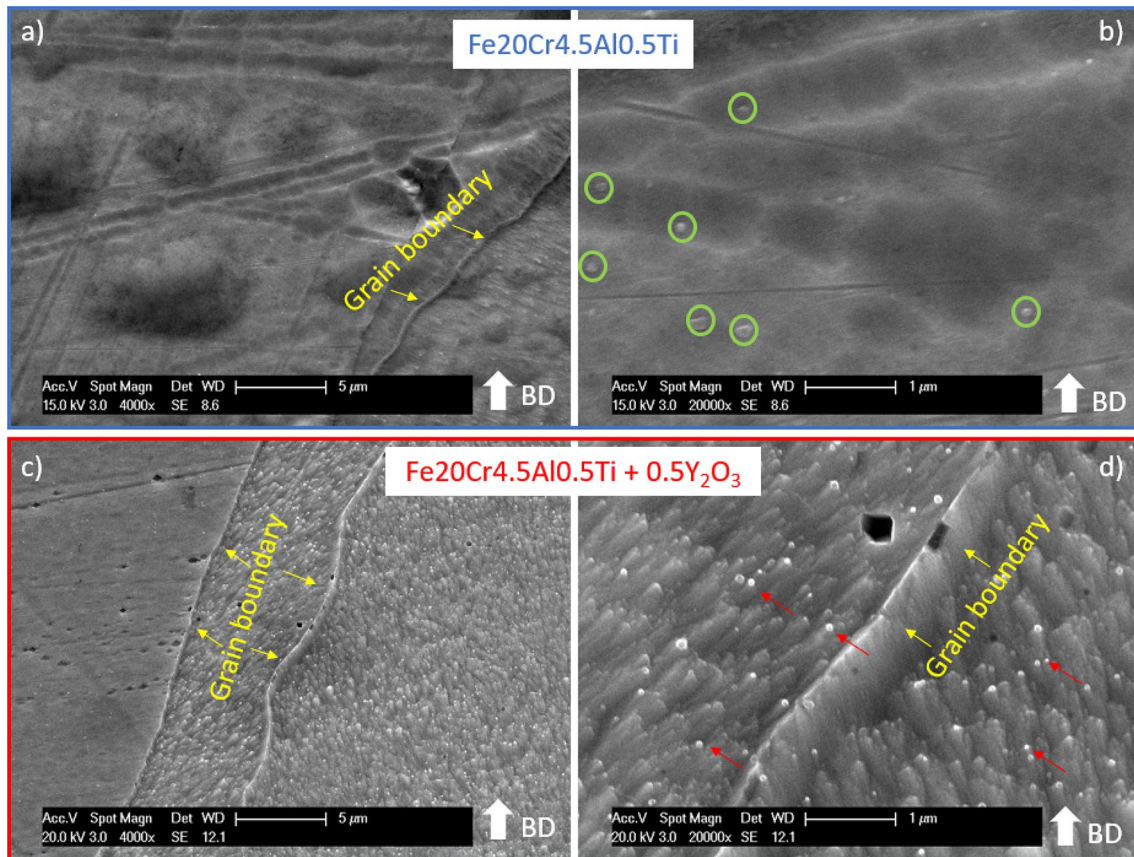
The microstructure of the non-reinforced material (Fe20Cr4.5Al0.5Ti) was examined using SEM images shown in Fig. 4a and is characterized by grain boundaries (marked with yellow arrows) in the build direction and a predominantly dendritic solidification structure. Within the microstructure, no precipitations or dispersoids can be detected (Fig. 4b). The sporadically observed flakes (green circles) could be identified as remnants of the etching process and were therefore discarded in the microstructure analysis.

SEM images of the reinforced material reveal the presence of sub-micrometer scaled oxide particles homogeneously distributed inside the grains, appearing as bright white spots throughout the microstructure (Fig. 4c). The microstructure evolution is not affected by the presence of the nanometer-scaled oxide particles, which are not acting as a site for heterogeneous nucleation of the ferritic matrix. This may be attributed to the low wettability of Y_2O_3 by iron–chromium melts [46]. The size of the nanoparticles (marked with red arrows) ranges between 50 and 150 nm (Fig. 4d). However, smaller nanoparticles may also be present, which cannot be resolved with the used SEM system. The nanoparticles are found to be significantly smaller than in PM2000 material processed via conventional DED (100–200 nm) [25] but larger than nanoparticles found in L-PBF processed with approx. 60 nm [21] and conventionally manufactured PM2000 with approx. 60 nm [47].

This process-related refinement of dispersed oxide particles can be further examined by modeling of the respective temperature distribution in the melt pool, the cooling rate, and the solidification rate encountered in the high-speed deposition process with the process parameters used (Table 2).

Comparing the calculated process-related values for HSLC with DED and L-PBF processes processing the same alloy, indicate that the considered values of maximum melt pool temperatures, solidification rates and cooling rates in HSLC are shifted from DED toward L-PBF (Table 3).

Fig. 4 SEM images of the microstructures of manufactured non-reinforced (**a**, **b**) and reinforced coatings (**c**, **d**)

Table 3 Maximum values for melt pool temperature, cooling rate, and solidification rate of DED, HSLC, and L-PBF

	DED [27]	HSLC	L-PBF [27]
Melt pool temperature [K]	3×10^3	2.6×10^3	2.3×10^3
Cooling rate [K/s]	6×10^4	1.1×10^6	2×10^6
Solidification rate [mm/s]	3×10^1	3.5×10^2	7×10^2

Values for DED and L-PBF are taken from [27], calculated with the identical mathematical model and material properties

The maximum melt pool temperature directly influences the melt viscosity and may enhance nano-particle mobility in the melt pool. Therefore, low melt pool temperatures are considered favorable for preventing nano-particle agglomeration. In Fig. 5c, high-temperature gradients in HSLC-formed melt pools are observed, which are believed to cause severe melt pool dynamics induced by maragoni convection, effectively preventing particle agglomeration. We hypothesize that even disruption of occasionally formed agglomerates by maragoni-induced shear forces might occur. Another factor for successful dispersion of nanoparticles is high cooling and solidification rates limiting the existence time of the melt pool significantly inhibiting diffusion controlled

agglomeration mechanisms [48]. Nanoparticles dispersed in the melt pool are instantaneously captured by the advancing solidification front and integrated in the mushy zone inhibiting the nanoparticles' mobility and therefore preventing agglomeration tendencies. Low solidification rates allow nanoparticles to agglomerate in the melt pool impeding capture by the mushy zone and are consequently being pushed in front of the solidification front [49]. Additionally, advanced particle agglomeration enforces buoyancy-induced flotation effects of nanoparticles leading to slag formation on the clads' surface and therefore reduced dispersion strengthening. [50] However, a direct comparison between the powder-blown deposition techniques of DED and HSLC, and the powder bed manufacturing process of L-PBF is difficult because of the strongly differing beam diameters (DED and HSLC: 0.66 mm [25], L-PBF: 0.08 mm [27]) leading to formation of increased melt pool dimensions in DED and HSLC, altering the solidification conditions significantly. The direct comparison of DED and HSLC with identical beam diameters used proves the ability to increase cooling and solidification rates leading to improved dispersion of nanoparticles in the stainless steel matrix reflected by smaller oxide particles in HSLC (50–150 nm) compared to DED (100–200 nm) [25].
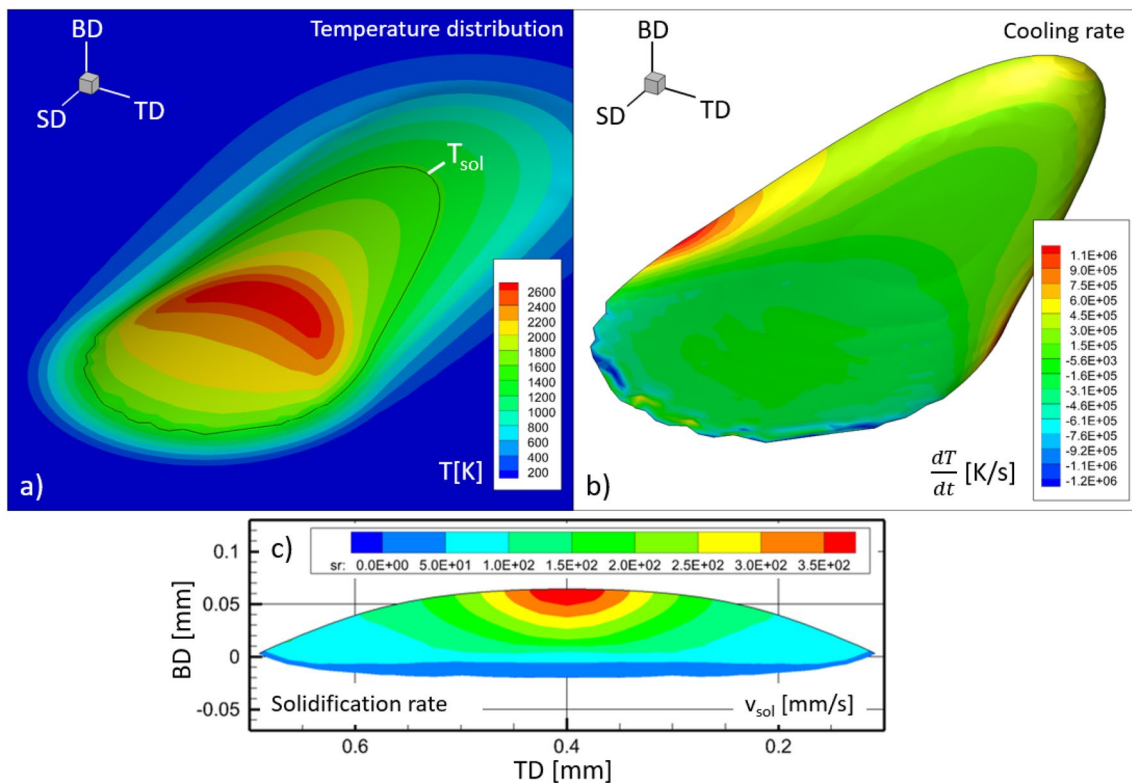
Fig. 5 Results of the FEM melt pool simulations. **a** Temperature distribution with laser movement in scanning direction (SD). The melt pool dimensions are indicated by the solidus temperature (T_{sol}). **b** Cooling rate in the solidification zone. Negative cooling rates can be considered as heating rates by the laser irradiation. **c** Solidification rate plotted in transverse (TD) and building direction (BD)
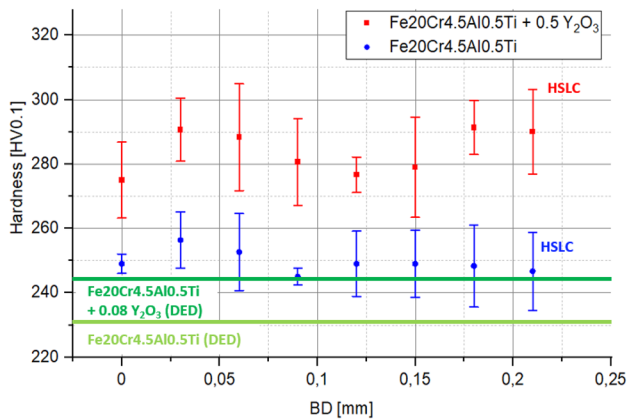
Fig. 6 Hardness profile over the building direction of Fe20Cr4.5Ti0.5 (blue) and Fe20Cr4.5Ti0.5 + 0.5% Y_2O_3 (red). Error bars indicate the respective standard deviation. Hardness measurements for DED-manufactured material (light and dark green lines) are taken from [54]

The chemical composition of the dispersoids in the ODS specimen could be evaluated using EDS analysis on rarely observable agglomerates, revealing enrichments of yttrium, oxygen and titanium. This indicates the formation of $Y_2Ti_2O_7$ or Y_2TiO_5 compounds typically found in titanium-alloyed Fe–Cr-based ODS steels [51]. The formation of Y–Al–O particles, found in Al-alloyed Fe–Cr-based ODS steels [52, 53], could not be observed. These findings are in agreement with DED-manufactured material. [25] However, a detailed study using high-resolution electron microscopy is necessary to confirm these results.

4.2 Mechanical characterization

The hardness profiles of both studied materials show a higher hardness of the reinforced material with hardnesses locally exceeding 300 HV0.1 (Fig. 6) proving the impact of nanoparticles on the hardness of the material. Please note that the nominal nano-particle mass loadings are different between the conventionally DED-manufactured sample (0.3 wt.%) [25, 54] and the HSLC (0.5 wt.%) processed material from this study.

However, the HSLC processed non-reinforced stainless steel (blue) exhibits a hardness of approx. 250 HV0.1, which is higher compared to its DED-manufactured specimen (approx. 230 HV0.1). Grain refinement enabled by higher solidification kinetics in the HSLC processed specimen may be a reason for this behavior. It can be concluded that nano-scaled dispersed oxides increase the hardness presumably by the Orowan mechanism leading to pronounced dispersoid hardening.

5 Conclusion

The feasibility of using the advanced DED process of high-speed laser cladding (HSLC) for the production of the Fe-based oxide-dispersion-strengthened alloy PM2000 has been demonstrated. Following major findings can be drawn from this study:

1) Manufacturing of defect-free specimens with low porosity using the high-speed laser cladding (HSLC) process was successful.
2) After HSLC processing, the reinforced PM2000 powder, a homogeneous distribution of sub-micrometer scaled Y–Ti–O-structured oxides within the metallic Fe20Cr4.5Al0.5Ti-matrix (wt.%), was achieved.
3) A considerable increase of hardness (approx. 320 HV0.1) of the reinforced PM2000 material was determined exceeding the hardness of the non-reinforced counterparts (approx. 260 HV0.1).

In-depth microstructural characterization using transmission electron microscopy (TEM) to clarify the crystallographic structure, size distribution and chemical composition of the nano-scaled oxides and electron backscatter diffraction (EBSD) examinations will be part of future studies to further characterize the local grain structure. Furthermore, mechanical characterizations for the determination of tensile and high-temperature properties will be performed.

Declarations

References

1. Odette GR, Alinger MJ, Wirth BD (2009) Recent developments in irradiation-resistant steels. Annu Rev Mater Res 38:471–503. https://doi.org/10.1146/annurev.matsci.38.060407.130315

2. Ukai S, Fujiwara M (2002) Perspective of ODS alloys application in nuclear environments. J Nucl Mater 307–311:749–757. https://doi.org/10.1016/S0022-3115(02)01043-7

3. Brodrick J, Hepburn DJ, Auckland GJ (2014) Mechanism for radiation damage resistance in yttrium oxide dispersion strengthened steels. J Nucl Mater 445:291–297. https://doi.org/10.1016/j.jnucmat.2013.10.045

4. Hoelzer DT, Bentley J, Solokov MA, Miller MK, Odette GR, Alinger MJ (2007) Influence of particle dispersions on the high temperature strength of ferritic alloys. J Nucl Mater 367–370:166–172. https://doi.org/10.1016/j.jnucmat.2007.03.151

5. Klueh RL, Maziasz PJ, Kim IS, Heatherly L, Hoelzer DT, Hashimoto N, Kenik EA, Miyahara K (2002) Tensile and creep properties of an oxide dispersion-strengthened ferritic steel. J Nucl Mater 307–311:773–777. https://doi.org/10.1016/S0022-3115(02)01046-2

6. Klueh RL, Shingledecker JP, Swindeman RW, Hoelzer DT (2005) Oxide dispersion-strengthened steels: a comparison of some commercial and experimental alloys. J Nucl Mater 341:103–114. https://doi.org/10.1016/j.jnucmat.2005.01.017

7. Wasilkowska A, Bartsch M, Messerschmidt U, Herzog R, Czyrska-Filemonowicz A (2003) Creep mechanisms of ferritic oxide dispersion strengthened alloys. J Mat Proc Techn 133:218–224. https://doi.org/10.1016/S0924-0136(02)00237-6

8. Mino K (1991) Development of ODS superalloy technology in Japan for turbine blade applications. J Eng Gas Turbines Power 113(4):568–573. https://doi.org/10.1115/1.2906279

9. Benjamin JS (1970) Dispersion strengthened superalloys by mechanical alloying. Met Trans 1:2943–2951. https://doi.org/10.1007/BF03037835

10. Suryanarayana C, Klassen T, Ivanov E (2011) Synthesis of nanocomposites and amorphous alloys by mechanical alloying. J Mater Sci 46:6301–6315. https://doi.org/10.1007/s10853-011-5287-0

11. Hilger I, Boulnat X, Hoffmann J, Testani C, Bergner F, de Carlan Y, Ferraro F, Ulbricht A (2016) Fabrication and characterization of oxide dispersion strengthened (ODS) 14Cr steels consolidated by means of hot isostatic pressing, hot extrusion and spark plasma sintering. J Nucl Mater 472:206–214. https://doi.org/10.1016/j.jnucmat.2015.09.036

12. Li Y, Shen J, Li F, Yang H, Kano S, Matsukawa Y, Satoh Y, Fu H, Abe H, Muroga T (2016) Effects of fabrication processing on the microstructure and mechanical properties of oxide dispersion strengthening steels. Mater Sci Eng A 654:203–212. https://doi.org/10.1016/j.msea.2015.12.032

13. Rieken J, Anderson IE, Kramer MJ, Odette GR, Stergar E, Haney E (2012) Reactive gas atomization processing for Fe-based ODS alloys. J Nucl Mater 428:65–75. https://doi.org/10.1016/j.jnucmat.2011.08.015

14. Tang H, Chen X, Chen M, Zuo L, Hou B, Wang Z (2014) Microstructure and mechanical property of in-situ nano-particle strengthened ferritic steel by novel internal oxidation. Mater Sci Eng A 609:293–299. https://doi.org/10.1016/j.msea.2014.05.020

15. Moghadasi MA, Nili-Ahmadabadi M, Forghani F, Kim HS (2016) Development of an oxide-dispersion-strengthened steel by introducing oxygen carrier compound into the melt aided by a general thermodynamic model. Sci Rep 6:38621. https://doi.org/10.1038/srep38621

16. Bergner F, Hilger I, Virta J, Lagerbom J, Gerbeth G, Connolly S, Hong Z, Grant PS, Weissgärber T (2016) Alternative fabrication routes towards oxide-dispersion-strengthened steels and model alloys. Metal & Mater Trans A 47:5313–5324. https://doi.org/10.1007/s11661-016-3616-2

17. Zhang H, Huang Y, Ning H, Williams CA, London AJ, Dawson K, Hong Z, Gorley MJ, Grovenor CRM, Tatlock GJ, Roberts SG, Reece MJ, Yan H, Grant PS (2015) Processing and microstructure characterization of oxide dispersion strengthened Fe-14Cr-0.4Ti-0.25Y$_2$O$_3$ ferritic steels fabricated by spark plasma sintering. J Nucl Mater 464:61–68. https://doi.org/10.1016/j.jnucmat.2015.04.029

18. Heintze C, Hernández-Mayoral M, Ulbricht A, Bergner F, Shariq A, Weissgärber T, Frielinghaus H (2012) Nanoscale characterization of ODS Fe-9%Cr model alloys compacted by spark plasma sintering. J Nucl Mater 428:139–146. https://doi.org/10.1016/j.jnucmat.2011.08.053

19. Boegelein T, Louvis E, Dawson K, Tatlock GJ, Jones AR (2016) Characterisation of a complex thin walled structure fabricated by selective laser melting using a ferritic oxide dispersion strengthened steel. Mater Charact 112:30–40. https://doi.org/10.1016/j.matchar.2015.11.021

20. Boegelein T, Dryepondt SN, Pandey A, Dawson K, Tatlock GJ (2015) Mechanical response and deformation mechanics of ferritic oxide dispersion strengthened steel structures produced by selective laser melting. Acta Mater 87:201–215. https://doi.org/10.1016/j.actamat.2014.12.047

21. Walker JC, Berggreen KM, Jones AR, Sutcliffe CJ (2009) Fabrication of Fe–Cr–Al Oxide dispersion strengthened PM2000 alloy using selective laser melting. Adv Eng Mater 11(7):541–546. https://doi.org/10.1002/ADEM.200800407

22. Hunt RM, Kramer KJ, El-Dasher B (2015) Selective laser sintering of MA956 oxide dispersion strengthened steel. J Nucl Mater 464:80–85. https://doi.org/10.1016/j.jnucmat.2015.04.011

23. Salman OO, Funk A, Waske A, Eckert J, Scudino S (2018) Additive manufacturing of a 316L steel matrix composite reinforced with CeO$_2$ particles: process optimization by adjusting the laser scanning speed. Technologies 6(1):25. https://doi.org/10.3390/technologies6010025

24. Kenel C, Dasargyri G, Bauer T, Colella A, Spierings AB, Leinenbach C, Wegener K (2017) Selective laser melting of an oxide dispersion strengthened (ODS) γ-TiAl alloy towards production of complex structures. Mater Des 134:81–90. https://doi.org/10.1016/j.matdes.2017.08.034

25. Streubel R, Wilms MB, Doñate-Buendía C, Weisheit A, Barcikowski S, Schleifenbaum JH, Gökce B (2018) Depositing laser-generated nanoparticles on powders for additive manufacturing of oxide dispersed strengthened alloy parts via laser metal deposition. Jap J Appl Phys 57(4):040310. https://doi.org/10.7567/JJAP.57.040310

26. Doñate-Buendía C, Streubel R, Kürnsteiner P, Wilms MB, Stern F, Tenkamp J, Bruder E, Barcikowski S, Gault B, Durst K, Schleifenbaum JH, Walther F, Gökce B (2020) Effect of nanoparticle additivation on the microstructure and microhardness of oxide dispersion strengthened steel produced by laser powder bed fusion and directed energy deposition. Proc CIRP 94:41–45. https://doi.org/10.1016/j.procir.2020.09.009

27. Doñate-Buendia C, Kürnsteiner P, Stern F, Wilms MB, Streubel R, Kusoglu IM, Tenkamp J, Bruder E, Pirch N, Barcikowski S, Durst K, Schleifenbaum JH, Walther F, Gault B, Gökce B (2021) Microstructure formation and mechanical properties of ODS steels built by laser additive manufacturing of nanoparticle coated iron-chromium powders. Acta Mater 206:116566. https://doi.org/10.1016/j.actamat.2020.116566

28. Wilms MB, Streubel R, Frömel F, Weisheit A, Tenkamp J, Walther F, Barcikowski S, Schleifenbaum JH, Gökce B (2018) Laser additive manufacturing of oxide dispersion strengthened steels using laser-generated nanoparticle-metal composite powders. Proc CIRP 74:196–200. https://doi.org/10.1016/j.procir.2018.08.093

29. Rittinghaus SK, Wilms MB (2019) Oxide dispersion strengthening of γ-TiAl by laser additive manufacturing. J All Comp 804:457–460. https://doi.org/10.1016/j.jallcom.2019.07.024

30. Arkhurst BM, Park JJ, Lee CH, Kim JH (2017) Direct laser deposition of 14Cr oxide dispersion strengthened steel powders using Y_2O_3 and HfO_2 dispersoids. Korean J Met Mater 55(8):550–558. https://doi.org/10.3365/KJMM.2017.55.8.550

31. Min Z, Parbat SN, Yang L, Kang B, Chyu MK (2018) Fabrication and characterisation of additive manufactured Nickel-based ODS coating layer for high temperature application. J Eng Gas Turbines Power 140(6):062101. https://doi.org/10.1115/1.4038351

32. Shi Y, Lu Z, Xu H, Xie R, Ren Y, Yang G (2019) Microstructure characterization and mechanical properties of laser additive manufactured oxide dispersion strengthened Fe-9Cr alloy. J All Comp 791:121–133. https://doi.org/10.1016/j.jallcom.2019.03.284

33. Shi Y, Lu Z, Yu L, Xie R, Ren Y, Yang G (2020) Microstructure and tensile properties of Zr-containing ODS-FeCrAl alloy fabricated by laser additive manufacturing. Mater Sci Eng A 774:138937. https://doi.org/10.1016/j.msea.2020.138937

34. Schmelzer J, Rittinghaus SK, Wilms MB, Michael O, Krüger M (2021) Strengthening of additively manufactured Me-Si-B (Me= Mo, V) by Y_2O_3 particles. Intern J Refract Met Hard Mater. 101:105623. https://doi.org/10.1016/j.ijrmhm.2021.105623

35. Schopphoven T, Gasser A, Backes G (2017) EHLA: extreme high-speed laser material deposition. Laser-Technik-J 14(4):26–29. https://doi.org/10.1002/latj.201700020

36. Zhong C, Pirch N, Gasser A, Poprawe R, Schleifenbaum JH (2017) The influence of powder stream on high-deposition-rate laser metal deposition with Inconel 718. Metals 7:443. https://doi.org/10.3390/met7100443

37. Schaible J, Sayk L, Schopphoven T, Schleifenbaum JH, Häfner C (2021) Development of a high-speed laser material deposition process for additive manufacturing. J Laser Appl 33:012021. https://doi.org/10.2351/7.0000320

38. Penttilä S, Toivonen A, Heikinheimo L, Novotny R (2010) Corrosion studies of candidate materials for European HPLWR. Nucl Techn 170:261–271. https://doi.org/10.13182/NT10-A9463

39. Koß S, Ewald S, Bold MN, Koch JH, Voshage M, Ziegler S, Schleifenbaum JH (2021) Comparison of the EHLA and LPBF process in context of new alloy design methods for LPBF. Adv Mater Res 1161:13–25. https://doi.org/10.4028/www.scientific.net/AMR.1161.13

40. Pirch N, Mokadem S, Keutgen S, Wissenbach K, Kreutz EW (2004) 3D-Model for laser cladding by powder injection. In: Geiger M, Otto A (eds) Laser assisted net shape engineering, vol 4. Meisenbach, Bamberg

41. Field KG, Snead MA, Yamamoto Y, Terrani KA (2018) Handbook on the material properties of FeCrAl alloys for nuclear power production applications. (FY Version: Revision 1), OSTI Technical Reports. https://doi.org/10.2172/1474581

42. Material data sheet: Kanthal APMT. https://www.kanthal.de/produkte-und-dienstleistungen/material-datasheets/wire/na/kanthal-apmt/?show=pdf. Accessed 30 Mar 2022

43. Pirch N, Keutgen S, Gasser A, Wissenbach K, Kelbassa I (2017) Modeling of coaxial single- and overlap-pass cladding with laser radiation. Proc. 37th MATADOR Conf. Manchester, UK. https://doi.org/10.1007/978-1-4471-4480-9_11

44. Pirch N, Linnenbrink S, Gasser A, Wissenbach K, Poprawe R (2017) Analysis of track formation during laser metal deposition. J Laser Appl 29:022506. https://doi.org/10.2351/1.4983231

45. Mokadem S, Bezençon C, Hauert A, Jacot A, Kurz W (2007) Laser repair of superalloy single crystals with varying substrate orientations. Met Mater Trans A 38:1500–1510. https://doi.org/10.1007/s11661-007-9172-z

46. Verhiest K, Mullens S, Paul J, De Graeve I, De Wispelaere N, Claessens S, DeBremaecker A, Verbeken K (2014) Experimental study on the contact angle formation of solidified iron–chromium droplets onto yttria ceramic substrates for the yttria/ferrous alloy system with variable chromium content. Ceram Int 40(1B):2187–2200. https://doi.org/10.1016/j.ceramint.2013.07.137

47. Shen YZ, Zhou TT, Zhang S, Sheng LZ (2013) Identification of oxide phases in oxide dispersion strengthened PM2000 steel. ISIJ Int 53(2):304–310. https://doi.org/10.2355/isijinternational.53.304

48. Verhiest K, Mullens S, De Wispelaere N, Claessens S, DeBremaecker A, Verbeken K (2012) Nano-yttria dispersed stainless steel composites composed by the 3 dimensional fiber deposition technique. J Nucl Mater 428:54–64. https://doi.org/10.1016/j.jnucmat.2012.01.025

49. Ferguson JB, Kaptay G, Schultz BF, Rohatgi PK, Cho K, Kim CS (2014) Brownian motion effects on particle pushing and engulfment during solidification in metal-matrix composites. Met Mater Trans A 45:4635–4645. https://doi.org/10.1007/s11661-014-2379-x

50. Yang Y, Doñate-Buendia C, Oyedeji TD, Gökce B, Xu BX (2021) Nanoparticle tracing during laser powder bed fusion of oxide dispersion strengthened steels. Materials 14(13):3463. https://doi.org/10.3390/ma14133463

51. Alinger MJ, Odette GR, Hoelzer DT (2009) On the role of alloy composition and processing parameters in the nanocluster formation and dispersion strengthening in nanostructured ferritic alloys. Acta Mater 57:392–406. https://doi.org/10.1016/j.actamat.2008.09.025

52. Klimenkov M, Lindau R, Möslang A (2007) Study of oxide precipitates in PM2000 steel. Microsc Microanal 13:296–297. https://doi.org/10.1017/S1431927607081482

53. Zhang ZB, Tao NR, Mishin OV, Pantleon W (2016) Oxide dispersion-strengthened steel PM2000 after dynamic plastic deformation: nanostructure and annealing behaviour. J Mater Sci 51:5545–5555. https://doi.org/10.1007/s10853-016-9859-x

54. Doñate-Buendia C, Frömel F, Wilms MB, Streubel R, Tenkamp J, Hupfeld T, Nachev M, Gökce E, Weisheit A, Barcikowski S, Walther F, Schleifenbaum JH, Gökce B (2018) Oxide dispersion-strengthened alloys generated by laser metal deposition of laser-generated nanoparticle-metal powder composites. Mater Des 154:360–369. https://doi.org/10.1016/j.matdes.2018.05.044